# Two-dimensional bipolar ferromagnetic semiconductors from layered antiferromagnets

Jun Deng,[1,2] Jiangang Guo,[1,3,*] Hideo Hosono,[4] Tianping Ying,[4] and Xiaolong Chen[1,2,3,†]

[1]*Beijing National Laboratory for Condensed Matter Physics, Institute of Physics, Chinese Academy of Sciences, Beijing 100190, China*

[2]*University of Chinese Academy of Sciences, Beijing 100049, China*

[3]*Songshan Lake Materials Laboratory, Dongguan, Guangdong 523808, China*

[4]*Materials Research Centre for Element Strategy, Tokyo Institute of Technology, Yokohama 226-8503, Japan*

(Received 8 November 2020; revised 24 January 2021; accepted 1 February 2021; published 15 March 2021)

Bipolar magnetic semiconductors (BMSs) are a class of compounds possessing different valence band maximum (VBM) and conduction band minimum (CBM) in terms of electron spins, which are related to but distinct from half-metals. They allow one to switch one spin current to another by applying external gate voltage or chemical doping, which can meet the requirement of bipolar manipulation in spintronic devices. Designing and searching BMSs are still a challenge. Here we predict that monolayer $CrPS_4$ and $CrPSe_4$ are bipolar ferromagnetic semiconductors with Curie temperature 58 K and 82 K, respectively. We predicted that they can be exfoliated from their A-type antiferromagnetic bulk form. Electric-field gating could drive $CrPS_4$ and $CrPSe_4$ into half-metals with reversible spin-polarization directions, where the bipolar doping is relatively easier to access for $CrPSe_4$ in experiment than $CrPS_4$ for its suitable electron affinity and ionic potential. Furthermore, we highlight the role played by the different magnitude between spin exchange splitting and crystal field splitting in the formation of BMSs. The results presented here may provide new clues in designing or searching BMSs.

DOI: 10.1103/PhysRevMaterials.5.034005

## I. INTRODUCTION

Spin-dependent transport of electrons has aroused intense interest recently for its potential applications in spintronics. Traditional half-metals could provide 100% spin-polarized current at one specific direction, which are candidate materials for such transport. Different from the fixed polarization of half-metals, conceptually, controlling the spin orientations of carriers and producing reversible polarized current by electrical-field control is more desirable in designing the next generation of devices compared with magnetic field control. Bipolar magnetic semiconductors (BMSs) are such a class of magnetic semiconductors in which the band structure splits into two subbands with different VBM and CBM, corresponding to electrons with two spin directions, respectively [1]. Applying a gate voltage or chemical doping could effectively tune the Fermi level and then adjust the orientations of spin current in a BMS. They have potential applications in spin filter, spin valve, or spin separators [1,2]. A few BMSs have been predicted by density functional theory, such as $MnPSe_3$ nanosheets [3], double perovskites $A_2CrOsO_6$ ($A$ = Ca, Sr, Ba) [4], Janus MXenes [5], and a DPP-based metal-organic framework [6]. Searching and designing experimental feasible BMSs with larger tunability and higher transition temperature remain a challenge.

The recent discovered layered transitional metal compounds have attracted much attention for their various magnetism. Their two-dimensional (2D) forms are highly desired for the miniaturization of spintronic devices. Typical examples are ferromagnetic (FM) monolayer $CrI_3$ [7] and bilayer $CrGeTe_3$ [8] with either the layer-dependent magnetism [7] or tunable magnetic ordering under external electric fields [9]. They are categorized as half semiconductors where the VBM and CBM have the same spin direction [10]. This is possibly due to the large on-site Coulomb repulsion of Cr-$d$ orbitals, which separates the spin-up and spin-down subbands far form each other and the energy gap locates between the $t_{2g}$ and $e_g$ orbitals opened by the crystal field in one spin channel. If manipulating the spin exchange interaction of Cr-$d$ orbitals or the strength of the crystal field to an ideal extent, a BMS would come into being. To realize such manipulation, we focus on the monolayers with ferromagnetism and semiconductivity in Cr-based layered compounds. As is well known, the monolayers usually keep their semiconducting behavior as their layered bulk form [7,11]. On the other hand, the spin alignment of monolayers can still keep the original magnetic state in the bulk crystal [7,12,13]. Thus, their bulk form could be either layered semiconducting ferromagnets or layered A-type antiferromagnets since their spins keep intralayer FM ordering. The former interlayer coupling is FM and the latter antiferromagnetic (AFM), but both interactions are so weak that they could be neglected in cleaving the monolayer counterpart.

In this article, we report that the exfoliation of the 2D form of $CrPS_4$, $CrPSe_4$, and $CrPTe_4$ from their A-type antiferromagnets is feasible. More importantly, the first two are revealed to be 2D bipolar ferromagnetic semiconductors and the last a conventional ferromagnetic semiconductor (FMS).

*jgguo@iphy.ac.cn
†xlchen@iphy.ac.cn

 

We show that the CBM and VBM possess opposite spin orientations in $CrPS_4$ and $CrPSe_4$ with typical features of BMSs. Either hole or electron doping by exertion of a gate voltage can turn them into half-metals with reversible spin-polarization directions. We think that bipolar doping in $CrPSe_4$ is easy to reach in experiment for its suitable electron affinity and ionic potential. Further analysis indicates that the difference between spin exchange splitting and crystal field splitting plays a key role in the formation of BMSs. Our results would stimulate experimental efforts to pursue the applications of BMSs in spintronics.

## II. COMPUTATIONAL METHODS

The first principles calculations were carried out with density functional theory (DFT) implemented in the Vienna *ab initio* simulation package (VASP) [14]. We adopted the generalized gradient approximation (GGA) in the form of the Perdew-Burke-Ernzerhof (PBE) [15] for the exchange-correlation potentials. The projector-augmented-wave (PAW) [16] pseudopotentials were used with a plane wave energy 500 eV. $3d^5 4s^1$ of Cr, $3s^2 3p^3$ of P, $3s^2 3p^4$ of S, $4s^2 4p^4$ of Se, and $5s^2 5p^4$ of Te electronic configurations were treated as valence electrons respectively. A Monkhorst-Pack Brillouin zone sampling grid [17] with a resolution $0.02 \times 2\pi$ Å$^{-1}$ was applied. The DFT+$U$ method introduced by Dudarev *et al.* [18] was used where mentioned. The Hubbard $U$ is applied to the Cr-$d$ orbitals. The van der Waals interaction was considered using DFT-D3 method of Grimme [19,20] for bulk $CrPX_4$ ($X$ = S, Se, Te). A vacuum layer of 20 Å was used to avoid the interlayer interactions along the $c$ direction for the monolayers. Atomic positions and lattice parameters were relaxed until all the forces on the ions were less than $10^{-3}$ eV/Å. Phonon spectra were calculated using the finite displacement method implemented in the PHONOPY code [21] to determine the lattice-dynamical stability of the structures and a $4 \times 4 \times 1$ supercell was adopted. *Ab initio* molecular dynamic (AIMD) simulations in the framework of the Nosé-Hoover thermostat ensemble were performed with time step 3 fs and lasting 9 ps, where a $2 \times 3 \times 1$ superlattice (containing 144 atoms) was used in the simulations and only Γ point was used in the Brillouin sampling. The hybrid functional HSE06 with a mixing parameter of 25% for the exact-exchange term was used to estimate the band gaps. Carrier doping was simulated by adding or removing extra electrons from the system, together with a compensating uniform homogeneous background charge. In calculating the magnetic anisotropic energy, the spin-orbit coupling (SOC) effect was included.

The classical Metropolis Monte Carlo (MC) simulations based on the Heisenberg model are used to estimate the magnetic transition temperatures. For bulk $CrPX_4$ ($X$ = S, Se, Te), a $40 \times 40 \times 40$ superlattice is used in our simulation and run $2 \times 10^7$ MC steps to reach the equilibrium state at each temperature. As for monolayer $CrPX_4$, a $50 \times 50$ superlattice is used and run $2 \times 10^7$ MC steps to reach the equilibrium state at each temperature. The specific heat is defined as $C_v = (\langle E^2 \rangle - \langle E \rangle^2)/(k_B T^2)$. The transition temperature is taken from the peak of specific heat.

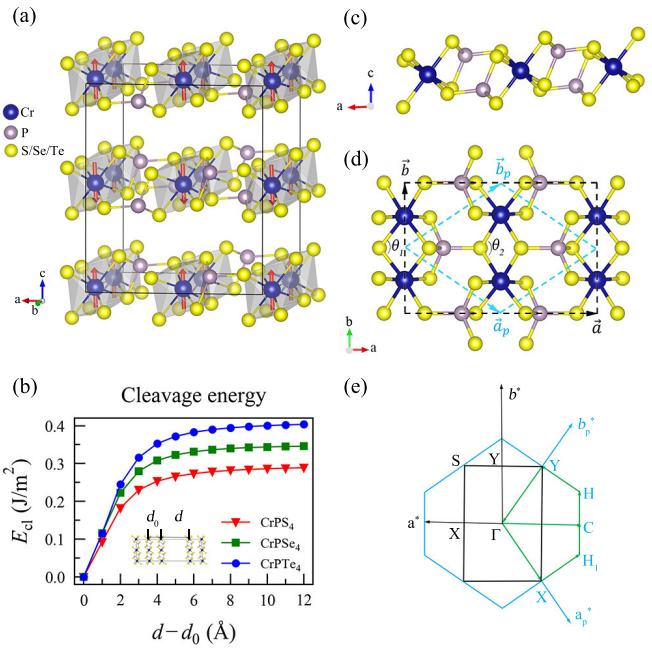


FIG. 1. (a) Crystal structure of bulk $CrPX_4$ ($X$ = S, Se, Te), the red arrows represent the calculated alignment of spins. (b) Cleavage energy ($E_{cl}$) as a function of separation distance ($d$-$d_0$) for $CrPX_4$ ($X$ = S, Se, Te), where $d$ is the separate distance and $d_0$ the distance between the layers at equilibrium state. (c–d) Crystal structure of monolayer $CrPX_4$ ($X$ = S, Se, Te) from side and top views, respectively. The blue dashed lines in (d) show the primitive cell of monolayer $CrPX_4$ defined by vector $\vec{a}_p$ and $\vec{b}_p$, and the black dashed lines are the conventional cell defined by vector $\vec{a}$ and $\vec{b}$. $\theta_1$ and $\theta_2$ are Cr-$X$-Cr angles. (e) The first Brillouin zone of monolayer $CrPX_4$. The black solid lines represent the folding of K points of the conventional lattice into the primitive cell. The VESTA [22] package was used to visualize the atomic structures.

## III. RESULTS AND DISCUSSION

### A. Bulk

Bulk $CrPS_4$ crystalizes with space group $C2/m$, lattice parameters $a = 10.871$ Å, $b = 7.254$ Å, $c = 6.140$ Å, and $\beta = 91.88°$ [23], shown in Fig. 1(a). It forms a layered structure stacking along the $c$ axis. Each layer consists of distorted $CrS_6$ octahedra and $PS_4$ tetrahedra. Bulk $CrPSe_4$ and $CrPTe_4$ are designed by completely replacing of S in $CrPS_4$ with Se and Te, respectively. The calculated lattice parameters are summarized in Table S1 [24]. Their magnetic structures are determined by comparing total energies of different possible magnetic structures shown in Fig. S1 [24] including the FM configuration. They exhibit A-type AFM orderings displayed in Fig. 1(a), where the magnetic moments of Cr are 2.81 $\mu_B$, 2.86 $\mu_B$, and 2.81 $\mu_B$ for $CrPS_4$, $CrPSe_4$, and $CrPTe_4$, respectively. Moreover, the estimated Néel temperatures ($T_N$s) using Monte Carlo simulations for $CrPS_4$, $CrPSe_4$, and $CrPTe_4$ are 37 K, 45 K, and 47 K, respectively; see Fig. S2 [24]. Then we calculated the formation enthalpies $\Delta H$ to evaluate the stability of $CrPSe_4$ and $CrPTe_4$. $\Delta H$ is defined as $\Delta H = (E_{CrPX_x} - E_{CrP} - xE_X)/(x+1)$, where $E_{CrPX_x}$, $E_{CrP}$, and $E_X$ are total energies for bulk $CrPX_x$, CrP, and $X$, respectively.

TABLE I. Optimized lattice constants (Å) of monolayer $CrPX_4$ ($X$ = S, Se, Te), relative energies (meV) of different magnetic structures in respect to the energy of ferromagnetism, and extracted coupling constants $J$ (meV) and $T_c$ (K) estimated by MC simulations.

| | a | b | $E_{FM}$ | $E_{AFM1}$ | $E_{AFM2}$ | $E_{AFM3}$ | $J_1$ | $J_2$ | $T_c$ |
|---|---|---|---|---|---|---|---|---|---|
| $CrPS_4$ | 10.873 | 7.346 | 0 | 28.24 | 137.59 | 102.159 | 3.82 | 0.78 | 58 |
| $CrPSe_4$ | 11.592 | 7.677 | 0 | 41.75 | 164.64 | 104.00 | 4.57 | 1.16 | 82 |
| $CrPTe_4$ | 12.833 | 8.062 | 0 | 149.30 | 300.16 | 112.591 | 8.34 | 4.15 | 193 |

The convex hull shown in Fig. S3 [24] indicates that both samples are stable in energy. Band structure calculations show that $CrPS_4$ is a direct band gap semiconductor, $CrPSe_4$ an indirect gap semiconductor and $CrPTe_4$ a metal; see Fig. S4 [24]. These results indicate that the PBE+D3 method could reproduce the correct experimental data [23,25–29] in lattice parameters, magnetic structure, magnetic moment, and $T_N$ for $CrPS_4$ except for the size of band gap. The calculated cleavage energies of $CrPX_4$ ($X$ = S, Se, Te) are 0.29 $J/m^2$, 0.35 $J/m^2$, 0.40 $J/m^2$, respectively [see Fig. 1(b)], which are comparable to or less than $0.32 \pm 0.03$ $J/m^2$ [30] for graphene, 0.24 $J/m^2$ for $MnPSe_3$ [3], 1.09 $J/m^2$ for $Ca_2N$ [31], and 0.30 $J/m^2$ for $CrI_3$ [32]. Thus, exfoliation of monolayer $CrPX_4$ from the bulky sample is highly feasible.

### B. Geometry and stability of monolayers

The structure of monolayer $CrPX_4$ ($X$ = S, Se, Te) is shown in Figs. 1(c) and 1(d). The optimized lattice parameters are summarized in Table I. The stability of monolayer $CrPS_4$ is discussed in other reports [33] and fabricated in Refs. [34,35], so we mainly examine the stability of monolayer $CrPSe_4$ and $CrPTe_4$ here. Both phonon spectra were calculated as shown in Fig. S5 [24]. No negative frequencies were observed, and they should be lattice-dynamically stable. The calculated elastic stiffness constants (Table S2 [24]) satisfy well the mechanical stability condition, $C_{11} > 0, C_{66} > 0$, $C_{11}C_{22} > C_{12}^2$ [36], indicating that they are mechanically stable. Moreover, the AIMD simulations for $CrPSe_4$ and $CrPTe_4$ were adopted to confirm their thermal stability at 300 K. The energy fluctuation shown in Fig. S6 [24] is small, revealing that they are also thermally stable at 300 K.

For a stable 2D monolayer, it must hold its own weight and geometry. The out-of-plane deformation $h$ due to gravity could be estimated by $h/L = (\rho g L/Y^{2D})^{1/3}$, where $L$ is the edge length of a square flake, $\rho$ density of a monolayer, $g$ the gravitational constant, and $Y^{2D}$ the Young's modulus. $Y^{2D}$ along the $\vec{a}$ and $\vec{b}$ directions can be deduced from the elastic constants by $Y_a^{2D} = (C_{11}C_{22} - C_{12}C_{21})/C_{11}$, and $Y_b^{2D} = (C_{11}C_{22} - C_{12}C_{21})/C_{22}$. For a typical value $L = 100\,\mu$m, the calculated $h/L$ of $CrPX_4$ ($X$ = S, Se, Te) are in an order of $10^{-4}$ listed in Table S3 [24], comparable to those of graphene [37] and $Ca_2N$ [31], suggesting that monolayer $CrPX_4$ is able to keep its free-standing plane structure under its own weight without substrate.

### C. Magnetic properties

Next, in order to determine the correct magnetic ground state, we compared the total energies of different magnetic structures of monolayer $CrPX_4$ ($X$ = S, Se, Te); see Fig. S7 [24]. As expected, monolayer $CrPX_4$ keeps FM alignment in the ground state. Here we assume that the spin configurations follow the classical Heisenberg Hamiltonian: $H = -J_1 \sum_{i,j} S_i S_j - J_2 \sum_{i,j} S_i S_j$, where $J_1$ is the nearest-neighbor and $J_2$ the next-nearest neighbor coupling constant. $J > 0$ indicates the coupling is FM. They could be extracted from the total energies of the above mentioned magnetic structures (see details in the Supplemental Material [24]). The results are shown in Table I. Then using these coupling parameters the $T_c$s are estimated by Monte Carlo simulations. All $T_c$ are higher than those of $CrI_3$ and bilayer $CrGeTe_3$; see Figs. 2(a) and 2(b).

Although the Mermin-Wagner theorem [38] demonstrates that the occurrence of magnetism for the isotropic Heisenberg model in a low dimension ($d \leqslant 2$) is forbidden, the

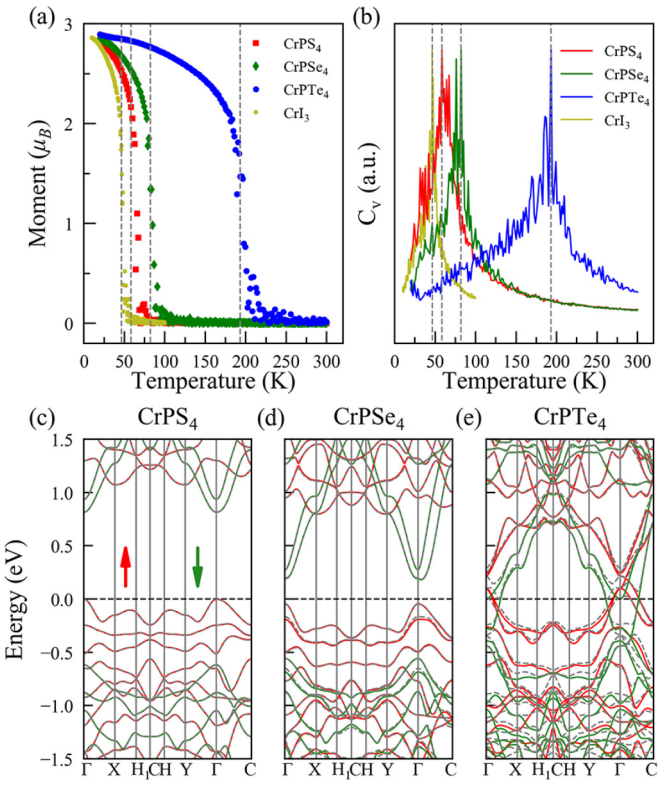


FIG. 2. Temperature-dependent (a) magnetic moment and (b) specific heat ($C_v$) for monolayer $CrPX_4$ ($X$ = S, Se, Te) based on Monte Carlo simulations. The result for $CrI_3$ is added for comparison, which agrees with the experimental value 45 K [7]. The dashed lines locate the $T_c$. (c–e) Spin-resolved electronic structures of monolayer $CrPS_4$, $CrPSe_4$, and $CrPTe_4$ with a PBE functional, respectively, where the Fermi level is set to be zero. The gray dashed lines show the band structures including spin-orbit coupling.

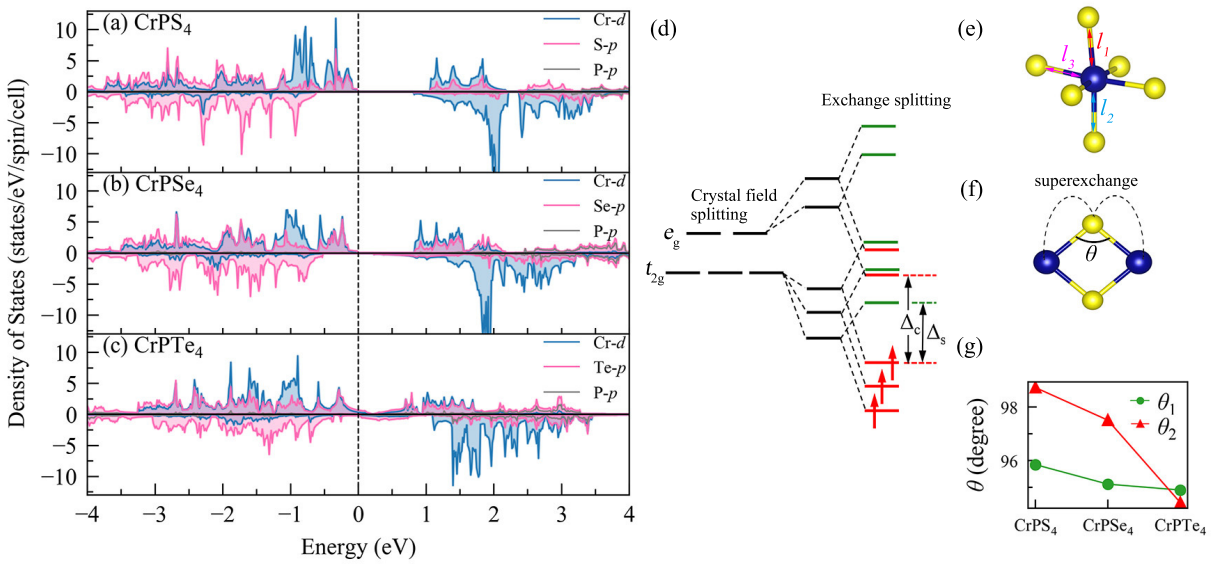


FIG. 3. Spin-resolved partial density of states of monolayer (a) $CrPS_4$, (b) $CrPSe_4$, and (c) $CrPTe_4$. (d) Schematic diagram of splitting and occupations of Cr-$d$ orbitals, where $\Delta_c$ is defined as the energy difference between VBM of spin-up channel and CBM of spin-up channel, and $\Delta_s$ the energy difference between the VBM of spin-up channel and CBM of spin-down channel. (e) Distorted $CrX_6$ octahedron in monolayer $CrPX_4$ ($X$ = S, Se, Te). $l_1$, $l_2$, and $l_3$ label the bond lengths of Cr-$X$ summarized in Table S4 [24]. (f) Schematic diagram of superexchange interactions of Cr-$X$-Cr. (g) Angles of Cr-$X$-Cr labeled in Fig. 1(d).

restriction could be broken by the emergence of large magnetic anisotropy. We calculated the angular dependent magnetic anisotropy energy (MAE), which is determined by rotating spins in the $xy/yz/xz$ planes. The results are illustrated in Fig. S8 [24]. Their MAE is nearly isotropic in the $xy$ plane but is strongly dependent on the direction of spin $\vec{s}$ in the $yz/xz$ plane. The easy axis of $CrPS_4$ is nearly toward the $z$ axis; it is close to an Ising magnet. While the easy axes of $CrPSe_4$ and $CrPTe_4$ are off the $z$ axis, $CrPSe_4$ is a weak XY ferromagnet and $CrPTe_4$ an anisotropic Heisenberg ferromagnet. All of them have sizable MAE, 53.25 $\mu$eV/Cr for $CrPS_4$, 223.28 $\mu$eV/Cr for $CrPSe_4$, and 2460.98 $\mu$eV/Cr for $CrPTe_4$, which is defined as the energy difference between easy axis and hard axis. The magnitude of MAE becomes stronger from $CrPS_4$ to $CrPTe_4$. This trend is caused by the SOC effect, which increases with $Z^4$ (Z: atomic number).

### D. Electronic structures

The electronic structures of monolayer $CrPX_4$ with a PBE functional are shown in Figs. 2(c)–2(e). The $CrPS_4$ and $CrPSe_4$ are FMSs and $CrPTe_4$ a ferromagnetic metal. The band structures including SOC correlation are also shown for comparison; see dashed lines in Figs. 2(c)–2(e). The influence of SOC increases from $CrPS_4$ to $CrPTe_4$. To get more accurate band structures for them, we resort to the HSE06 functional and include SOC correction for $CrPTe_4$. A narrow band gap ~64.3 meV shows up for $CrPTe_4$ as exhibited in Fig. S9(c) [24]. More interestingly, we have found that both $CrPS_4$ and $CrPSe_4$ belong to the category of BMSs [1] under a PBE functional, where the CBM and VBM possess different spin channels. Considering the strong correlation of Cr-$d$ orbitals, we also investigate the influence of Hubbard $U$ on the band structures of $CrPS_4$ and $CrPSe_4$ by the DFT+$U$ method. As shown in Fig. S10 [24], the CBM changes its spin direction for $CrPS_4$ as $U$ larger than 1.6 eV while it has no influence on the $CrPSe_4$ with $U$ up to 3 eV. Also by using HSE06 functional, $CrPS_4$ becomes a half semiconductor; see Fig. S9(a) [24]. These results indicate that the BMS feature is not robust for $CrPS_4$ while $CrPSe_4$ is a good BMS.

To further understand the electronic and magnetic properties of $CrPX_4$ ($X$ = S, Se, Te), the densities of states (DOS) are calculated as shown in Figs. 3(a)–3(c). There is a large spin splitting in the $d$ orbitals of Cr atoms seen from the DOS plots, contributing to the magnetism. This is also verified by the calculated magnetic density, which mainly localized at Cr atoms; see Fig. S11(a)–S11(c) [24]. The charge density difference map [Figs. S11(d)–S11(f) [24]] reveals that Cr and P lose electrons while S/Se/Te gains electrons. Due to the octahedral crystal field of Cr atoms, the energy levels of $d$ orbitals will split into two groups $t_{2g}$ ($d_{xy}$, $d_{yz}$, $d_{xz}$) and $e_g$ ($d_{x^2-y^2}$, $d_{z^2}$) with a splitting gap $\Delta_c$. The degeneracy of these energy levels will be removed because of the distorted octahedral crystal field [Fig. 3(e)] in $CrPX_4$. Then, due to the on-site Coulomb repulsion of Cr-$d$ orbitals, these energy levels will further split into two subbands, spin up and spin down, with a spin exchange splitting gap $\Delta_s$. According to the electronegativity and nominal valence state $Cr^{3+}$, three electrons occupy the $t_{2g}$ orbitals of spin-up subbands, consistent with the calculated magnetic moment 3 $\mu_B$/formula. Figure 3(d) shows the energy splitting and occupations of Cr-3$d$ orbitals. The band gap $\Delta_c$ in the spin-up channel decreases from $CrPS_4$ to $CrPTe_4$, which relates to the weakened crystal field effect. The exchange splitting $\Delta_s$ is largely dependent on the on-site Coulomb repulsion of Cr-$d$ orbitals. The feature of BMSs in $CrPS_4$ and $CrPSe_4$ is attributed to the large crystal field effect and low on-site Coulomb repulsion of Cr-$d$ orbitals, which result in $\Delta_c > \Delta_s$ in these systems.

The magnetic ordering could be understood on the basis of the superexchange interactions. The spin-up channel shows that there is a large overlap between Cr-$d$ and $X$-$p$ ($X$ = S/Se/Te) orbitals in the DOS plots Figs. 3(a)–3(c), while the overlap between Cr-$d$ and P-$p$ is small, implying that $X$-$p$ orbitals play an important role in determining the magnetic exchange interactions. According to the Goodenough-Kanamori-Anderson rules [39–41], if 3$d$ transition metal cations are connected at 90° by a nonmagnetic anion, the magnetic interaction is FM. While if the relative angle is larger than 90°, the FM interaction will be weakened due to the competition between AFM and FM interaction. The angles of Cr-$X$-Cr summarized in Fig. 3(g) are only slightly larger than 90° and nearly meet the ideal angle 90° for FM superexchange interaction. Both angles ($\theta_1$ and $\theta_2$) decrease from $CrPS_4$ to $CrPTe_4$, leading to the increment of magnetic coupling constant $J_1$ through Cr-$X$-Cr superexchange. As for the next-neighbor exchange interaction $J_2$, it is mediated by $PX_4$ tetrehedra and would be weaker due to the longer distance between Cr atoms. The electron localization function (ELF) in Figs. S11(g)–S11(i) [24] shows that the electron density at $PX_4$ ($X$ = S, Se, Te) unit increases from S to Te, indicating the enhanced superexchange interaction $J_2$. As a result, the $T_c$ increases from $CrPS_4$, $CrPSe_4$, to $CrPTe_4$.

### E. Manipulation of BMSs by doping

The energy differences between FM and other AFM configurations are calculated against different carrier doping concentrations; see Figs. 4(a) and 4(b). Over the whole doping region, the FM configuration is the most favored state. Figure 4(c) illustrates how doping possibly changes the band structures and spin orientation of electrons (see details in Fig. S12 [24]). With hole doping, the spin-up carriers dominate the Fermi level, and they can keep half-metallicity as $n$ up to $4 \times 10^{14}$ cm$^{-2}$; on the other hand, with electron doping, the spin-down carriers dominate the Fermi level, but they will lose the half-metallic state when the $n$ is above $2 \times 10^{14}$ cm$^{-2}$.

It should be noted that in a semiconductor, the key to achieve bipolar manipulation in experiment is the magnitudes of electron affinity (EA, $E_{CBM} - E_{vac}$) and ionization potential (IP, $E_{VBM} - E_{vac}$). Here the $E_{vac}$ is the vacuum energy. It is well documented that electron doping can be realized when EA is lower than −3.8 eV and hole doping when IP higher than −6 eV [42,43]. For example, substantial attempts demonstrate that doping electrons into ZnO is rather easy but hole doping is difficult [44]. The critical factor is that the IP is too deep. On the contrary, the electron doping of $Cu_2O$ is hard for its shallow EA. Thus, we calculated EA and IP for $CrPS_4$ and $CrPSe_4$. Figure 4(d) shows the band alignments of $CrPS_4$, $CrPSe_4$, and other typical nonmagnetic semiconductors. In this respect, it seems that monolayer $CrPSe_4$ is easier to realize for bipolar doping in experiment since the VBM and CBM locate at −6.05 eV and −4.77 eV, respectively, lying in the idea energy range.

Here we propose to use external electric field to reversibly tune the spin-polarization directions. As previously reported, in a field-effect-transistor encapsulated monolayer $MoS_2$, the mobility can be largely promoted by two orders of magnitude, possibly due to suppression of Coulomb scattering under the high-$\kappa$ dielectric environment [45]. Moreover, the AFM state of bilayer $CrI_3$ can switch to the FM state under the electric field, which is the consequence of change of interlayer potential induced by the magnetoelectric effect [9]. Compared to the traditional field effect technique, the ionic-liquid gating method can largely enhance the carrier concentration from $10^{13}$ to $10^{15}$ cm$^{-2}$ [46]. Utilizing this technique, the $T_c$ of monolayer $Fe_3GeTe_2$ was enhanced up to 310 K, in which the gated electrons fill the lower bands of Fe-3$d$ states, leading to a sharp peak in the density of states at the $E_f$ and the increment of $T_c$ [12]. Thus fabrication of monolayer $CrPX_4$ and examination of bipolar ferromagnetism under external electric field deserve an experimental investigation.

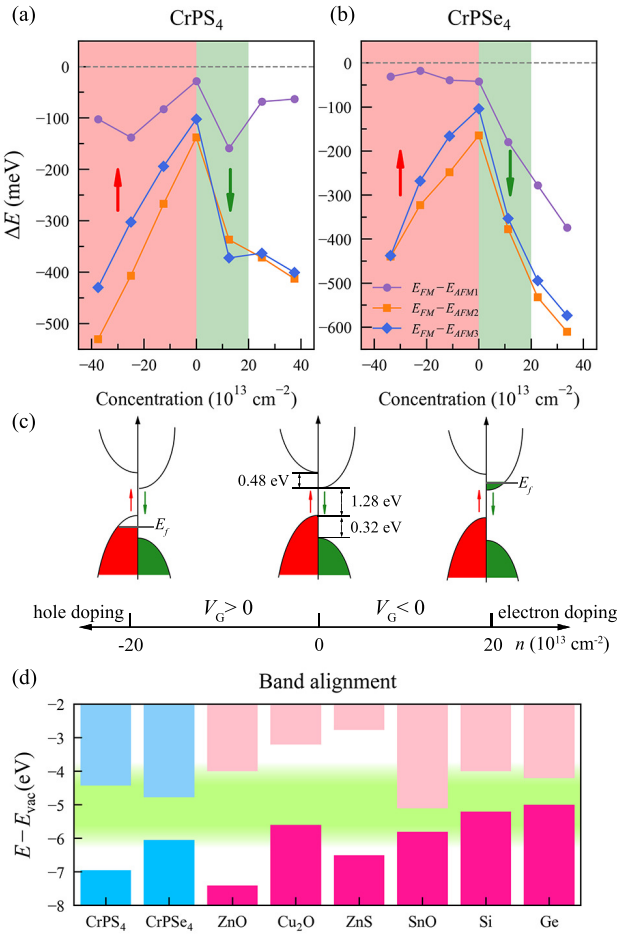


FIG. 4. (a, b) Energy differences between the FM and AFM1, AFM2, and AFM3 configurations as a function of doping carrier concentrations for $CrPS_4$ and $CrPSe_4$, respectively. The up and down arrows indicate that electrons across the Fermi level are spin-up and spin-down electrons, respectively, corresponding to red and green regions. The other region means that electrons of both spins occupy the Fermi level. (c) Manipulation of spin orientations by gate voltage. The middle picture shows the three energy band gaps of $CrPSe_4$ calculated with an HSE06 functional. (d) Band alignment of $CrPX_4$ ($X$ = S, Se) calculated with an HSE06 functional together with other reported typical semiconductors shown for comparison; relevant data are taken from Ref. [42]. The green region indicates the bipolar doping windows.

TABLE II. Predicted carrier mobility $\mu$ ($cm^2\ V^{-1}\ S^{-1}$) at 300 K.

| | Direction | $\mu_e$ | $\mu_h$ |
|---|---|---|---|
| $CrPS_4$ | $\vec{a}$ | 10.4080 | 2.7332 |
| | $\vec{b}$ | 220.3679 | 64.0766 |
| $CrPSe_4$ | $\vec{a}$ | 69.6392 | 9.7457 |
| | $\vec{b}$ | 832.6568 | 99.1692 |

### F. Mobility

For practical applications, the mobility of semiconductors is a key factor influencing the performance. The acoustic phonon-limited carrier mobility is estimated by deformation potential (DP) theory; see detailed methods in the Supplemental Material [24]. The obtained results at $T = 300$ K are summarized in Table II. The electron mobility is higher than hole mobility for both $CrPS_4$ and $CrPSe_4$ at either direction. Moreover, the Cr atoms bond tighter in the $\vec{b}$ direction than the $\vec{a}$ direction, leading to anisotropy in transport properties. Both of them have comparable or higher mobility than monolayer $MoS_2$ [47].

### G. Mechanism for BMSs

Finally, we discuss the general formation mechanism of bipolar ferromagnetic semiconductors. Two energy gaps, $\Delta_c$ and $\Delta_s$, determine whether the ferromagnetic semiconductor is a BMS, which relates to the strength of crystal field and on-site Coulomb repulsion. Only when the crystal field splitting $\Delta_c$ is larger than spin exchange splitting $\Delta_s$ does the band feature of BMSs come into being. Hence, reducing spin exchange splitting or enhancing the crystal field effect is an effective way to design new BMSs. Usually, $4d/5d$ transition metals have smaller exchange splitting than $3d$ transition metals at the same crystal field. For example, when substituting Cr with Mo or W in monolayer $CrGeTe_3$, it transforms from a half semiconductor to a BMS and then an FM metal; see Fig. S13 [24]. This method is successfully applied to $NbS_2$ and $ReS_2$ [48,49]. In enhancing the crystal field effect, two rules should be mainly considered: the energy splitting of octahedral crystal field is usually larger than that of tetrahedral crystal field; stronger bonding between metal and ligands favors larger splitting. Here is a brief guideline to design new BMSs: (1) choose metals with a high group number (e.g. $4d/5d$ transition metal) to reduce the spin exchange splitting; (2) choose ligands with larger electronegativity to achieve strong bonding with metals; (3) ensure that they are in an octahedral crystal field. Apart from this, alloying $3d/5d$ transition metals [10] or mixing ligands with different electronegativity [50] in a same structure is also possible to approach BMSs. With these strategies, we hope more BMSs can be screened and designed.

## IV. CONCLUSIONS

In summary, we identified monolayer $CrPS_4$ and $CrPSe_4$ as new 2D bipolar ferromagnetic semiconductors and $CrPTe_4$ a regular ferromagnetic semiconductor that are exfoliated from their A-type layered bulk antiferromagnets. The small cleavage energies and weak interlayer magnetic coupling ensure the intralayer FM alignments of Cr under the 2D limit. In particular, $CrPS_4$ and $CrPSe_4$ can transform to half-metals with opposite spin-polarization directions by applying an external gate voltage. Furthermore, $CrPSe_4$ can easily reach bipolar doping for its suitable electron affinity and ionic potential. Our work emphasizes that the strength of on-site Coulomb repulsion and crystal field plays an important role in the formation of BMSs. This kind of carrier concentration dependent magnetism provides intriguing opportunities for the fundamental research and potential application of spintronic devices.

## ACKNOWLEDGMENTS

This work is financially supported by the MoST-Strategic International Cooperation in Science, Technology and Innovation Key Program (2018YFE0202601); the National Key Research and Development Program of China (2017YFA0304700, 2016YFA0300600); the National Natural Science Foundation of China under Grants No. 51772322 and 51922105; the Key Research Program of Frontier Sciences, CAS, Grant No. QYZDJ-SSW-SLH013; and the Beijing Natural Science Foundation (Grant No. Z200005).

[1] X. Li, X. Wu, Z. Li, J. Yang, and J. G. Hou, Nanoscale **4**, 5680 (2012).
[2] L. L. Tao and E. Y. Tsymbal, Phys. Rev. B **100**, 161110(R) (2019).
[3] X. Li, X. Wu, and J. Yang, J. Am. Chem. Soc. **136**, 11065 (2014).
[4] X. X. Li, X. J. Wu, Z. Y. Li, and J. L. Yang, Phys. Rev. B **92**, 125202 (2015).
[5] J. J. He, P. B. Lyu, L. Z. Sun, A. M. Garcia, and P. Nachtigall, J. Mater. Chem. C **4**, 6500 (2016).
[6] X. Li and J. Yang, J. Phys. Chem. Lett. **10**, 2439 (2019).
[7] B. Huang, G. Clark, E. Navarro-Moratalla, D. R. Klein, R. Cheng, K. L. Seyler, D. Zhong, E. Schmidgall, M. A. McGuire, D. H. Cobden *et al.*, Nature (London) **546**, 270 (2017).
[8] C. Gong, L. Li, Z. Li, H. Ji, A. Stern, Y. Xia, T. Cao, W. Bao, C. Wang, Y. Wang *et al.*, Nature (London) **546**, 265 (2017).
[9] S. Jiang, J. Shan, and K. F. Mak, Nat. Mater. **17**, 406 (2018).
[10] C. Huang, J. Feng, F. Wu, D. Ahmed, B. Huang, H. Xiang, K. Deng, and E. Kan, J. Am. Chem. Soc. **140**, 11519 (2018).
[11] K. F. Mak, C. Lee, J. Hone, J. Shan, and T. F. Heinz, Phys. Rev. Lett. **105**, 136805 (2010).
[12] Y. Deng, Y. Yu, Y. Song, J. Zhang, N. Z. Wang, Z. Sun, Y. Yi, Y. Z. Wu, S. Wu, J. Zhu *et al.*, Nature (London) **563**, 94 (2018).
[13] G. Long, H. Henck, M. Gibertini, D. Dumcenco, Z. Wang, T. Taniguchi, K. Watanabe, E. Giannini, and A. F. Morpurgo, Nano Lett. **20**, 2452 (2020).
[14] G. Kresse and J. Furthmuller, Comput. Mater. Sci. **6**, 15 (1996).
[15] J. P. Perdew, K. Burke, and M. Ernzerhof, Phys. Rev. Lett. **77**, 3865 (1996).

[16] G. Kresse and D. Joubert, Phys. Rev. B **59**, 1758 (1999).

[17] H. J. Monkhorst and J. D. Pack, Phys. Rev. B **13**, 5188 (1976).

[18] S. L. Dudarev, G. A. Botton, S. Y. Savrasov, C. J. Humphreys, and A. P. Sutton, Phys. Rev. B **57**, 1505 (1998).

[19] S. Grimme, J. Antony, S. Ehrlich, and H. Krieg, J. Chem. Phys. **132**, 154104 (2010).

[20] S. Grimme, S. Ehrlich, and L. Goerigk, J. Comput. Chem. **32**, 1456 (2011).

[21] A. Togo and I. Tanaka, Scr. Mater. **108**, 1 (2015).

[22] K. Momma and F. Izumi, J. Appl. Crystallogr. **44**, 1272 (2011).

[23] Q. L. Pei, X. Luo, G. T. Lin, J. Y. Song, L. Hu, Y. M. Zou, L. Yu, W. Tong, W. H. Song, W. J. Lu, and Y. P. Sun, J. Appl. Phys. **119**, 043902 (2016).

[24] See Supplemental Material at http://link.aps.org/supplemental/10.1103/PhysRevMaterials.5.034005 for magnetic structures of bulk and monolayer $CrPX_4$; Monte Carlo simulations of bulk and monolayer $CrPX_4$; convex hull; band structures of bulk and monolayer $CrPX_4$; phonon spectra and AIMD simulations of $CrPX_4$; spin charge, charge density difference, and ELF of monolayer $CrPX_4$; optimized structure parameters of monolayer $CrPX_4$; elastic constants, Young's modulus, and bond length of monolayer $CrPX_4$; structure information for monolayer $CrPX_4$; and details of estimation of coupling constants and mobility, which includes Refs. [10,47,51].

[25] H. Wu and H. Chen, RSC Adv. **9**, 30655 (2019).

[26] A. K. Budniak, N. A. Killilea, S. J. Zelewski, M. Sytnyk, Y. Kauffmann, Y. Amouyal, R. Kudrawiec, W. Heiss, and E. Lifshitz, Small **16**, 1905924 (2020).

[27] S. Calder, A. V. Haglund, Y. Liu, D. M. Pajerowski, H. B. Cao, T. J. Williams, V. O. Garlea, and D. Mandrus, Phys. Rev. B **102**, 024408 (2020).

[28] Y. X. Peng, S. L. Ding, M. Cheng, Q. F. Hu, J. Yang, F. G. Wang, M. Z. Xue, Z. Liu, Z. C. Lin, M. Avdeev *et al.*, Adv. Mater. **32**, 8 (2020).

[29] A. Louisy, G. Ouvrard, D. M. Schleich, and R. Brec, Solid State Commun. **28**, 61 (1978).

[30] R. Zacharia, H. Ulbricht, and T. Hertel, Phys. Rev. B **69**, 155406 (2004).

[31] S. T. Zhao, Z. Y. Li, and J. L. Yang, J. Am. Chem. Soc. **136**, 13313 (2014).

[32] M. A. McGuire, H. Dixit, V. R. Cooper, and B. C. Sales, Chem. Mater. **27**, 612 (2015).

[33] H. L. Zhuang and J. Zhou, Phys. Rev. B **94**, 195307 (2016).

[34] J. Lee, T. Y. Ko, J. H. Kim, H. Bark, B. Kang, S.-G. Jung, T. Park, Z. Lee, S. Ryu, and C. Lee, ACS Nano **11**, 10935 (2017).

[35] S. Kim, J. Lee, G. Jin, M. H. Jo, C. Lee, and S. Ryu, Nano Lett. **19**, 4043 (2019).

[36] M. Maździarz, 2D Mater. **6**, 048001 (2019).

[37] T. J. Booth, P. Blake, R. R. Nair, D. Jiang, E. W. Hill, U. Bangert, A. Bleloch, M. Gass, K. S. Novoselov, M. I. Katsnelson, and A. K. Geim, Nano Lett. **8**, 2442 (2008).

[38] N. D. Mermin and H. Wagner, Phys. Rev. Lett. **17**, 1133 (1966).

[39] J. Kanamori, J. Appl. Phys. **31**, S14 (1960).

[40] P. W. Anderson, Phys. Rev. **115**, 2 (1959).

[41] J. B. Goodenough, Phys. Rev. **100**, 564 (1955).

[42] H. Hosono, Jpn. J. Appl. Phys. **52**, 090001 (2013).

[43] T. Arai, S. Iimura, J. Kim, Y. Toda, S. Ueda, and H. Hosono, J. Am. Chem. Soc. **139**, 17175 (2017).

[44] A. Janotti and C. G. Van de Walle, Rep. Prog. Phys. **72**, 126501 (2009).

[45] B. Radisavljevic, A. Radenovic, J. Brivio, V. Giacometti, and A. Kis, Nat. Nanotechnol. **6**, 147 (2011).

[46] A. S. Dhoot, C. Israel, X. Moya, N. D. Mathur, and R. H. Friend, Phys. Rev. Lett. **102**, 136402 (2009).

[47] Y. Cai, G. Zhang, and Y.-W. Zhang, J. Am. Chem. Soc. **136**, 6269 (2014).

[48] Y. Sun, Z. Zhuo, and X. Wu, J. Mater. Chem. C **6**, 11401 (2018).

[49] Z. Sun, H. Lv, Z. Zhuo, A. Jalil, W. Zhang, X. Wu, and J. Yang, J. Mater. Chem. C **6**, 1248 (2018).

[50] F. Zhang, W. Mi, and X. Wang, Adv. Electron. Mater. **6**, 1900778 (2020).

[51] J. Xi, M. Long, L. Tang, D. Wang, and Z. Shuai, Nanoscale **4**, 4348 (2012).